Gust Load Alleviation Control and Gust Estimation for a High Aspect Ratio Wing Wind Tunnel Model

Christopher Forte*
KBR Wyle, Inc., Moffett Field, CA 94035
Nhan Nguyen†
NASA Ames Research Center, Moffett Field, CA 94035
Juntao Xiong‡
KBR Wyle, Inc., Moffett Field, CA 94035

This paper presents the gust load alleviation (GLA) study of the aspect ratio 13.5 Common Research Model (CRM) wind-tunnel model. This study details the design of the GLA controller in preparation for wind-tunnel testing in the Transonic Dynamics Tunnel at NASA Langley Research Center. An aeroservolastic (ASE) model was first reduced using a model reduction method that takes advantage of the sinusoidal steady-state response. Then, the reduced model was used to design an extended-state Kalman filter which estimates the states and the sinusoidal gust input. The GLA control was then derived using the optimal control solution to a multi-objective cost function. The results of the GLA controller indicate a 75.6% **reduction in wing-root strain while maintaining robust stability margins. The final paper will include performance under sub-optimal conditions, e.g., sensor noise, uncertainty in gust frequency, etc..**

I. Introduction

The aircraft industry has been redesigning modern aircraft in response to the demand for more energy-efficient aircraft. Some design considerations of these aircraft are redesigning airframes to be aerodynamically and structurally more efficient, employing lightweight composite materials for aircraft structures, and incorporating more energy-efficient aircraft engines. The reduction of airframe operational empty weight is one of the major considerations for improving energy efficiency. The Boeing 787, for example, is a modern aircraft that employs advanced lightweight composite materials. These modern materials, however, can provide less structural rigidity while maintaining sufficient load carrying capacity. As structural flexibility increases, aeroelastic interactions with aerodynamic forces can adversely affect aircraft performance. The increase in wing aspect ratio also exacerbates the aeroelastic problem as the wing twist under load can be substantial. These advancements in wing structure can make the aircraft more vulnerable to aeroelastic disturbances such as wind gusts. One approach for reducing the impact of gust disturbances on the airframe is using an active control system. Forward looking LIDAR systems are currently in development to estimate the gust upstream of a moving aircraft. These gust estimates may then be incorporated into the active flight control system with the objective of reducing the loads on aircraft structure.

This paper explores gust load alleviation (GLA) control strategy for an aspect ratio 13.5 Common Research Model (CRM) wind-tunnel model developed by Boeing under a NASA contract with the Integrated Adaptive Wing Technology Maturation (IAWTM) program funded by NASA Advanced Air Transport Technology (AATT) project. The aspect ratio 13.5 CRM is developed from the original aspect ratio 8.3 CRM.[1] Figure 1 illustrates the aspect ratio 13.5 CRM configuration. The IAWTM team is preparing for a test at the NASA Langley Research Center (LaRC) in the Transonic Dynamics Tunnel (TDT). There, the team will investigative active flight controls on a 10.8 % scale model wing and half fuselage. The model is a half-span, wall-mounted, aeroelastically-scaled model of the CRM with an aspect ratio of 13.5. This configuration employs a distributed mini-plain flap system which comprises 7 mini-plain flaps (MPFs) and 3 ailerons positioned along the wing trailing edge. The wind tunnel model configuration can be seen in Figure 2. These MPFs and ailerons can be used for active control strategies. These strategies include real-time drag optimization,

*Aerospace Engineer, Intelligent System Division, christopher.j.forte@nasa.gov, AIAA Member
†Senior Research Scientist and Technical Group Lead, Intelligent Systems Division, nhan.t.nguyen@nasa.gov, Associate Fellow AIAA
‡Aerospace Engineer, Intelligent System Division, juntao.xiong@nasa.gov, AIAA Member

maneuver load alleviation,[2] and gust load alleviation control designs which will be experimentally verified in the TDT. The TDT is equipped with an Airstream Oscillation System (AOS) which is comprised of two sets of gust vane paddles located upstream of the test section. This system can be seen in Fig. 3 The gust vane paddles oscillate at a chosen frequency to produce a sinusoidal gust disturbance. A gust sniffer, which is located upstream of the wind tunnel model, takes measurements of the gust as a surrogate to the LIDAR systems in development. The ultimate goal of the GLA tests is to reduce the inboard strain gauge measurements, particularly the strain gauge closest to the wing root, when the GLA controller is active compared to when the GLA controller is inactive.

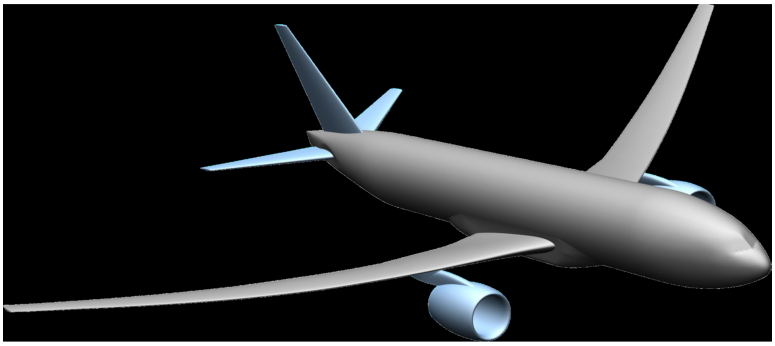

Figure 1 Common Research Model (CRM) Concept[3]

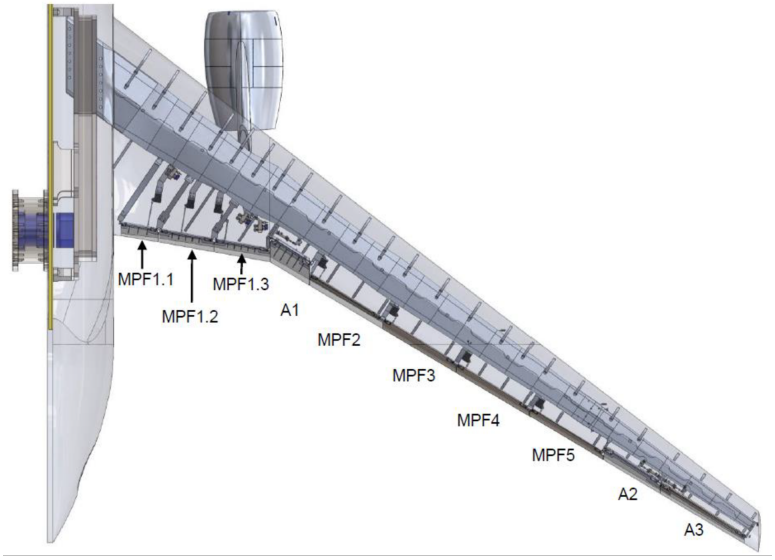

Figure 2 Wind Tunnel Model Configuration[3]

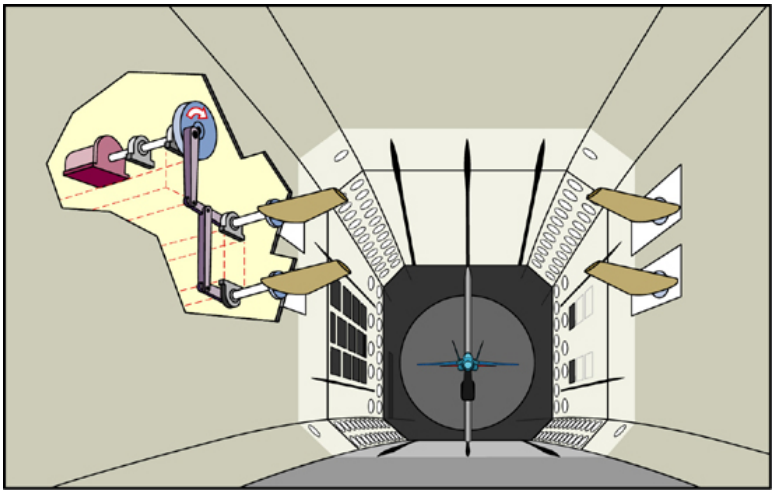

Figure 3 Wind Tunnel Model Configuration[4]

A multi-objective flight control system for flexible aircraft equipped with distributed flight control surfaces has been developed by NASA to simultaneously achieve aerodynamic efficiency, ASE mode suppression, and gust/maneuver load alleviation while maintaining traditional pilot command-tracking tasks for guidance and navigation.[5–11] The multi-objective flight control framework comprises the following objectives all acting in a synergistic manner: 1) traditional pilot command-following flight control, 2) drag minimization, 3) aeroelastic mode suppression, and 4) gust/maneuver load alleviation. Ride quality improvement objective can also be incorporated in this framework by leveraging the gust aeroelastic mode suppression and gust load alleviation capabilities. Fig. 4 illustrates an architecture of a multi-objective flight control system. The GLA controller being developed is a subset of this multi-objective flight control framework where the cost function only includes the load performance objective as shown:[5]

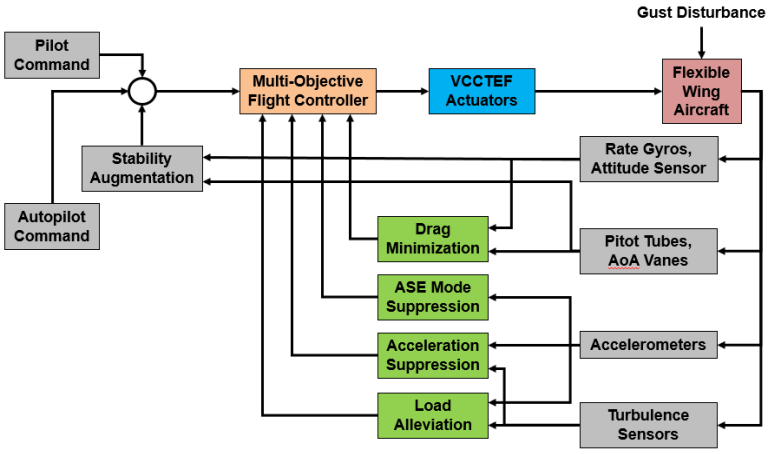

Figure 4 Multi-Objective Flight Control Framework[9]

The objective of this study is to develop a GLA controller for the CRM wind-tunnel model for the upcoming IAWTM testing that would reduce the wing-root strain gauge measurement while the model experiences a gust disturbance. The state-space aeroservolastic (ASE) model from which the GLA controller was designed, representing the CRM model under wind-tunnel test conditions, was provided by NASA LaRC. This model was reduced using a technique

that takes advantage of the sinusoidal steady-state system response to a sinusoidal gust input. Then, an extended-state Kalman filter was designed to estimate the states and gust. The GLA controller is then derived using an optimal control approach, where the controller is obtained by optimizing a multi-objective cost function which includes a term for the root strain gauge measurement. This resulted in a state feedback controller with a feedforward term corresponding to the gust states. The robustness of the controller was analyzed by computing the stability margins of the controller. It is particularly important to ensure robust stability margins to account for the uncertainty in the analytical model compared to the real model in the wind-tunnel environment. Lastly, the controller is tested via a MATLAB simulation.

II. Model Reduction

A. Aeroservolastic Model

The ASE state-space model was developed by NASA LaRC,[12] using the software ZAERO and a NASTRAN finite element analysis model. The model is partitioned into modal states, control surface actuator states, and gust vane states. Similarly, the control input can be partitioned into the actuator control input, and gust vane control input.

$$\begin{bmatrix} \dot{x}_m \\ \dot{x}_a \\ \dot{x}_g \end{bmatrix} = \begin{bmatrix} A_{mm} & A_{ma} & A_{mg} \\ 0 & A_{aa} & 0 \\ 0 & 0 & A_{gg} \end{bmatrix} \begin{bmatrix} x_m \\ x_a \\ x_g \end{bmatrix} + \begin{bmatrix} 0 & 0 \\ B_a & 0 \\ 0 & B_g \end{bmatrix} \begin{bmatrix} u_a \\ u_c \end{bmatrix} \tag{1}$$

$$y = \begin{bmatrix} C_m & C_a & C_g \end{bmatrix} \begin{bmatrix} x_m \\ x_a \\ x_g \end{bmatrix} \tag{2}$$

The gust dynamics are then treated separately

$$\begin{bmatrix} \dot{x}_m \\ \dot{x}_a \end{bmatrix} = \begin{bmatrix} A_{mm} & A_{ma} \\ 0 & A_{aa} \end{bmatrix} \begin{bmatrix} x_m \\ x_a \end{bmatrix} + \begin{bmatrix} 0 \\ B_a \end{bmatrix} u_c + \begin{bmatrix} A_{mg} \\ 0 \end{bmatrix} x_g \tag{3}$$

$$y = \begin{bmatrix} C_m & C_a \end{bmatrix} \begin{bmatrix} x_m \\ x_a \end{bmatrix} + C_g x_g \tag{4}$$

$$\dot{x}_g = A_{gg} x_g + B_g u_g \tag{5}$$

or a system in the form

$$\dot{x} = Ax + Bu + Ew \tag{6}$$

$$y = Cx + Fw \tag{7}$$

where w is treated as a disturbance input.

The CRM wind-tunnel model is equipped with many sensors available for use for use in controller design. Of the wide range of sensors include 16 accelerometers and 10 full-bridge strain gauges. Of the 16 accelerometers, 3 are 3-axis accelerometers and 13 are 1-axis accelerometers oriented in the z-direction. Thus, there is a total of 22 accelerometer signals available to the control system. These sensors, amongst others, are modeled as outputs to the ASE model. The location of the strain gauges and accelerometers are depicted in Fig. 5.

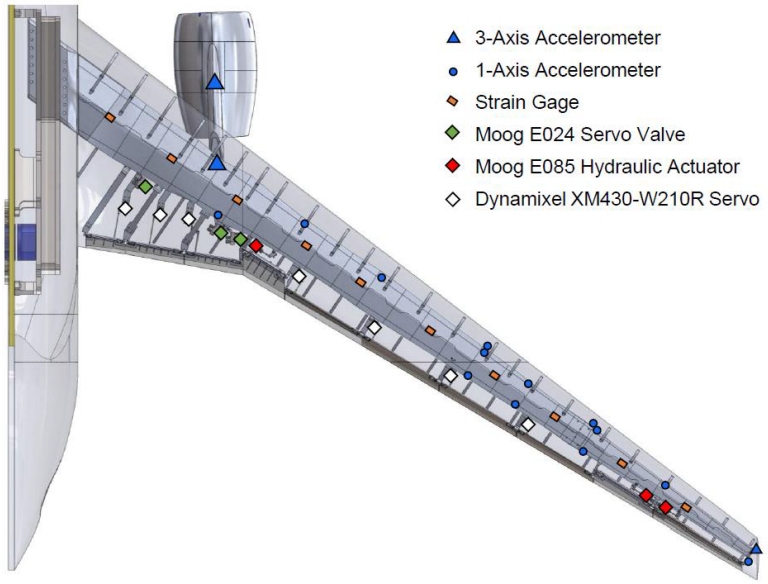

Figure 5 Common Research Model Sensors[3]

B. Model Reduction Process

The ASE model, in the form represented by Eq. 6 and Eq. 7, can be partitioned into modal states x_s, aerodynamic lag states x_l, and actuator states x_a

$$\begin{bmatrix} \dot{x}_s \\ \dot{x}_l \\ \dot{x}_a \end{bmatrix} = \begin{bmatrix} A_{ss} & A_{sl} & A_{sa} \\ A_{ls} & A_{ll} & A_{la} \\ 0 & 0 & A_{aa} \end{bmatrix} \begin{bmatrix} x_s \\ x_l \\ x_a \end{bmatrix} + \begin{bmatrix} 0 \\ 0 \\ B_a \end{bmatrix} u + \begin{bmatrix} E_s \\ E_l \\ 0 \end{bmatrix} w \tag{8}$$

$$y = \begin{bmatrix} C_s & C_l & C_a \end{bmatrix} \begin{bmatrix} x_s \\ x_l \\ x_a \end{bmatrix} + Fw \tag{9}$$

Furthermore, we can separate the modal states into modal displacements, x_e and modal rates $\dot{x}_e$, the actuator states into actuator displacements x_A and actuator rates $\dot{x}_A$, and the gust states into gust displacements W and gust rates $\dot{W}$, such that:

$$x_s = \begin{bmatrix} x_e \\ \dot{x}_e \end{bmatrix} \tag{10}$$

$$x_a = \begin{bmatrix} x_A \\ \dot{x}_A \end{bmatrix} \tag{11}$$

and

$$w = \begin{bmatrix} W \\ \dot{W} \end{bmatrix} \tag{12}$$

We first look to remove the aerodynamic lag states. The dynamics of the aerodynamic lag states x_l are written as

$$\dot{x}_l = A_{ll}x_l + A_{ls}x_s + A_{la}x_a + E_l w \tag{13}$$

Furthermore, this equation can be written as

$$\dot{x}_l = A_{ll}x_l + A_{ls_1}x_e + A_{ls_2}\dot{x}_e + A_{la_1}x_A + A_{la_2}\dot{x}_A + E_{l_1}W + E_{l_2}\dot{W} \tag{14}$$

The steady-state responses of the aerodynamic lag states, modal states, actuator states, and the gust states are assumed to be sinusoidal and therefore can be expressed as

$$x_l = a_1 \sin\omega_g t + a_2 \cos\omega_g t \tag{15}$$

$$x_e = b_1 \sin\omega_g t + b_2 \cos\omega_g t \tag{16}$$

$$x_A = c_1 \sin\omega_g t + c_2 \cos\omega_g t \tag{17}$$

$$W = d_1 \sin\omega_g t + d_2 \cos\omega_g t \tag{18}$$

Substituting into the aerodynamic lag state equation (Eq. 14) yields

$$\begin{aligned}\dot{x}_l = a_1\omega_g \cos\omega_g t - a_2\omega_g \sin\omega_g t = A_{ll}(a_1 \sin\omega_g t + a_2 \cos\omega_g t) + A_{ls_1}(b_1 \sin\omega_g t + b_2 \cos\omega_g t)\\ +A_{ls_2}(b_1\omega_g \cos\omega_g t - b_2\omega_g \sin\omega_g t) + A_{la_1}(c_1 \sin\omega_g t + c_2 \cos\omega_g t)\\ +A_{la_2}(c_1\omega_g \cos\omega_g t - c_2\omega_g \sin\omega_g t) + E_{l_1}(d_1 \sin\omega_g t + d_2 \cos\omega_g t)\\ +E_{l_2}(d_1\omega_g \cos\omega_g t - d_2\omega_g \sin\omega_g t)\end{aligned} \tag{19}$$

We then obtain

$$-A_{ll}a_1 - a_2\omega_g = A_{ls_1}b_1 - A_{ls_2}b_2\omega_g + A_{la_1}c_1 - A_{la_2}c_2\omega_g + E_{l_1}d_1 - E_{l_2}d_2\omega_g \tag{20}$$

$$a_1\omega_g - A_{ll}a_2 = A_{ls_1}b_2 + A_{ls_2}b_1\omega_g + A_{la_1}c_2 + A_{la_2}c_1\omega_g + E_{l_1}d_2 + E_{l_2}d_1\omega_g \tag{21}$$

Solving for a_1 and a_2 yields

$$\begin{bmatrix} a_1 \\ a_2 \end{bmatrix} = \begin{bmatrix} -A_{ll} & -\omega_g \\ \omega_g & -A_{ll} \end{bmatrix}^{-1} \begin{bmatrix} A_{ls_1}b_1 - A_{ls_2}b_2\omega_g + A_{la_1}c_1 - A_{la_2}c_2\omega_g + E_{l_1}d_1 - E_{l_2}d_2\omega_g \\ A_{ls_1}b_2 + A_{ls_2}b_1\omega_g + A_{la_1}c_2 + A_{la_2}c_1\omega_g + E_{l_1}d_2 + E_{l_2}d_1\omega_g \end{bmatrix} \tag{22}$$

$$\begin{aligned}a_1 = \alpha_{11}(A_{ls_1}b_1 - A_{ls_2}b_2\omega_g + A_{la_1}c_1 - A_{la_2}c_2\omega_g + E_{l_1}d_1 - E_{l_2}d_2\omega_g)\\ +\alpha_{12}(A_{ls_1}b_2 + A_{ls_2}b_1\omega_g + A_{la_1}c_2 + A_{la_2}c_1\omega_g + E_{l_1}d_2 + E_{l_2}d_1\omega_g)\end{aligned} \tag{23}$$

$$\begin{aligned}a_2 = \alpha_{21}(A_{ls_1}b_1 - A_{ls_2}b_2\omega_g + A_{la_1}c_1 - A_{la_2}c_2\omega_g + E_{l_1}d_1 - E_{l_2}d_2\omega_g)\\ +\alpha_{22}(A_{ls_1}b_2 + A_{ls_2}b_1\omega_g + A_{la_1}c_2 + A_{la_2}c_1\omega_g + E_{l_1}d_2 + E_{l_2}d_1\omega_g)\end{aligned} \tag{24}$$

But

$$\alpha_{11} = \alpha_{22} \tag{25}$$

$$\alpha_{12} = -\alpha_{21} \tag{26}$$

So

$$\begin{aligned}a_1 = \alpha_{11}(A_{ls_1}b_1 - A_{ls_2}b_2\omega_g + A_{la_1}c_1 - A_{la_2}c_2\omega_g + E_{l_1}d_1 - E_{l_2}d_2\omega_g)\\ +\alpha_{12}(A_{ls_1}b_2 + A_{ls_2}b_1\omega_g + A_{la_1}c_2 + A_{la_2}c_1\omega_g + E_{l_1}d_2 + E_{l_2}d_1\omega_g)\end{aligned} \tag{27}$$

$$\begin{aligned}a_2 = -\alpha_{12}(A_{ls_1}b_1 - A_{ls_2}b_2\omega_g + A_{la_1}c_1 - A_{la_2}c_2\omega_g + E_{l_1}d_1 - E_{l_2}d_2\omega_g)\\ +\alpha_{11}(A_{ls_1}b_2 + A_{ls_2}b_1\omega_g + A_{la_1}c_2 + A_{la_2}c_1\omega_g + E_{l_1}d_2 + E_{l_2}d_1\omega_g)\end{aligned} \tag{28}$$

Substituting Eq. 27 and Eq. 28 into Eq. 15, expanding and examining terms containing b_1 and b_2 we obtain

$$\begin{aligned}x_l = \ldots + \alpha_{11}A_{ls_1}b_1 \sin\omega_g t + \alpha_{11}A_{ls_1}b_2 \cos\omega_g t + \alpha_{11}A_{ls_2}b_1\omega_g \cos\omega_g t - \alpha_{11}A_{ls_2}b_2\omega_g \sin\omega_g t\\ -\alpha_{12}A_{ls_1}b_1 \cos\omega_g t + \alpha_{12}A_{ls_1}b_2 \sin\omega_g t + \alpha_{12}A_{ls_2}b_1\omega_g \sin\omega_g t + \alpha_{12}A_{ls_2}b_2\omega_g \cos\omega_g t + \ldots\\ = \ldots + \alpha_1 b_1 \sin\omega_g t + \alpha_1 b_2 \cos\omega_g t - \alpha_2 b_1 \cos\omega_g t + \alpha_2 b_2 \sin\omega_g t\\ -\alpha_3 b_1 \cos\omega_g t + \alpha_3 b_2 \cos\omega_g t + \alpha_4 b_1 \sin\omega_g t + \alpha_4 b_2 \cos\omega_g t + \ldots\\ = \ldots + \alpha_1 x_e + \alpha_2 \frac{1}{\omega_g}\dot{x}_e + \alpha_3 \frac{1}{\omega_g}\dot{x}_e + \alpha_4 x_e + \ldots\end{aligned} \tag{29}$$

$$\alpha_1 x_e + \alpha_2 \frac{1}{\omega_g}\dot{x}_e + \alpha_3 \frac{1}{\omega_g}\dot{x}_e + \alpha_4 x_e = \bar{\alpha}_1 x_e + \bar{\alpha}_2 \dot{x}_e = \begin{bmatrix} \bar{\alpha}_1 & \bar{\alpha}_2 \end{bmatrix} \begin{bmatrix} x_e \\ \dot{x}_e \end{bmatrix} = K_1 x_s \tag{30}$$

Differentiating this term

$$\frac{d}{dt}(K_1 x_s) = \bar{\alpha}_1 \dot{x}_e + \bar{\alpha}_2 \ddot{x}_e \tag{31}$$

But

$$\ddot{x}_e = -\omega_g^2 x_e \tag{32}$$

$$\frac{d}{dt}(K_1 x_s) = \bar{\alpha}_1 \dot{x}_e - \bar{\alpha}_2 \omega_g^2 x_e = \begin{bmatrix} \bar{\alpha}_1 & \bar{\alpha}_2 \end{bmatrix} \begin{bmatrix} 0 & I \\ -\omega_g I & 0 \end{bmatrix} \begin{bmatrix} x_e \\ \dot{x}_e \end{bmatrix} = K_1 K_g x_s \tag{33}$$

We can similarly write the other terms when substituting Eq. 27 and Eq. 28 into Eq. 15 in a similar form. We can then write the lag state in terms of the modal states, actuator states, and gust states

$$x_l = K_1 x_s + K_2 x_a + K_3 w \tag{34}$$

and

$$\dot{x}_l = K_1 K_g x_s + K_2 K_g x_a + K_3 K_g w \tag{35}$$

We may then substitute Eq. 34 and Eq. 35 into Eq. 13

$$\dot{x}_l = K_1 K_g x_s + K_2 K_g x_a + K_3 K_g w = A_{ll}(K_1 x_s + K_2 x_a + K_3 w) + A_{ls} x_s + A_{la} x_a + E_l w \tag{36}$$

We can then form the following Sylvester equations, from which we can solve for K_1, K_2, and K_3

$$K_1 K_g - A_{ll} K_1 = A_{ls} \tag{37}$$

$$K_2 K_g - A_{ll} K_2 = A_{la} \tag{38}$$

$$K_3 K_g - A_{ll} K_3 = E_l \tag{39}$$

We can rewrite the system in Eq. 8 and Eq. 9 by substituting for x_l using Eq. 34

$$\dot{x}_s = A_{ss} x_s + A_{sl}(K_1 x_s + K_2 x_a + K_3 w) + A_{sa} x_a + E_s w \tag{40}$$

$$\dot{x}_s = (A_{ss} + A_{sl} K_1) x_s + (A_{sa} + A_{sl} K_2) x_a + (E_s + A_{sl} K_3) w \tag{41}$$

$$y = C_s x_s + C_l(K_1 x_s + K_2 x_a + K_3 w) + C_a x_a + F w \tag{42}$$

$$y = (C_s + C_l K_1) x_s + (C_a + C_l K_2) x_a + (F + C_l K_3) w \tag{43}$$

Organizing in Matrix form we have

$$\begin{bmatrix} \dot{x}_s \\ \dot{x}_a \end{bmatrix} = \begin{bmatrix} A_{ss} + A_{sl} K_1 & A_{sa} + A_{sl} K_2 \\ 0 & A_{aa} \end{bmatrix} \begin{bmatrix} x_s \\ x_a \end{bmatrix} + \begin{bmatrix} 0 \\ B_a \end{bmatrix} u + \begin{bmatrix} E_s + A_{sl} K_3 \\ 0 \end{bmatrix} w \tag{44}$$

$$y = \begin{bmatrix} C_s + C_l K_1 & C_a + C_l K_2 \end{bmatrix} \begin{bmatrix} x_s \\ x_a \end{bmatrix} (F + C_l K_3) w \tag{45}$$

We can also use the same approach to reduce the high frequency modes that may be outside the bandwidth of the actuators, or may have relatively low impact on the system response. We can separate the modal states into states we want to retain x_r and fast states we want to remove x_f. The above system can be written as

$$\dot{x}_R = A_R x_R + B_R u + E_R w \tag{46}$$

$$y_R = C_R x_R + F_R w \tag{47}$$

Separating the system into states we want to retain, states we want to remove, and actuator states

$$\begin{bmatrix} \dot{x}_r \\ \dot{x}_f \\ \dot{x}_a \end{bmatrix} = \begin{bmatrix} A_{rr} & A_{rf} & A_{ra} \\ A_{fr} & A_{ff} & A_{fa} \\ 0 & 0 & A_{aa} \end{bmatrix} \begin{bmatrix} x_r \\ x_f \\ x_a \end{bmatrix} + \begin{bmatrix} 0 \\ 0 \\ B_a \end{bmatrix} u + \begin{bmatrix} E_r \\ E_f \\ 0 \end{bmatrix} w \tag{48}$$

$$y_R = \begin{bmatrix} C_r & C_f & C_a \end{bmatrix} \begin{bmatrix} x_r \\ x_f \\ x_a \end{bmatrix} + F_R w \tag{49}$$

Similarly to removing the lag states, we can write the states we wish to remove x_f in terms of the other states

$$x_f = K_4 x_r + K_5 x_a + K_6 w \tag{50}$$

and

$$\dot{x}_f = K_4 K_g x_r + K_5 K_g x_a + K_6 K_g w \tag{51}$$

We write $\dot{x}_f$ as

$$\dot{x}_f = A_{fr} x_r + A_{ff} x_f + A_{fa} x_a + E_f w \tag{52}$$

Which then becomes

$$K_4 K_g x_r + K_5 K_g x_a + K_6 K_g w = A_{fr} x_r + A_{ff}(K_4 x_r + K_5 x_a + K_6 w) + A_{fa} x_a + E_f w \tag{53}$$

Which results in the following Sylvester equations from which K_4, K_5, and K_6 can be solved

$$K_4 K_g - A_{ff} K_4 = A_{fr} \tag{54}$$

$$K_5 K_g - A_{ff} K_5 = A_{fa} \tag{55}$$

$$K_6 K_g - A_{ff} K_6 = E_f \tag{56}$$

We write the states we want to retain as

$$\dot{x}_r = A_{rr} x_r + A_{rf} x_f + A_{ra} x_a + E_r w \tag{57}$$

Substituting for x_f (Eq. 50)

$$\dot{x}_r = A_{rr} x_r + A_{rf}(K_4 x_r + K_5 x_a + K_6 w) + A_{ra} x_a + E_r w \tag{58}$$

$$\dot{x}_r = (A_{rr} + A_{rf} K_4) x_r + (A_{ra} + A_{rf} K_5) x_a + (E_r + A_{rf} K_6) w \tag{59}$$

We write the output equation as

$$y_R = C_r x_r + C_f x_f + C_a x_a + F_R w \tag{60}$$

Substituting for x_f (Eq. 50)

$$y_R = C_r x_r + C_f(K_4 x_r + K_5 x_a + K_6 w) + C_a x_a + F_R w \tag{61}$$

$$y_R = (C_r + C_f K_4) x_r + (C_a + C_f K_5) x_a + (F_R + C_f K_6) w \tag{62}$$

In matrix form the system becomes

$$\begin{bmatrix} \dot{x}_r \\ \dot{x}_a \end{bmatrix} = \begin{bmatrix} A_{rr} + A_{rf}K_4 & A_{ra} + A_{rf}K_5 \\ 0 & A_{aa} \end{bmatrix} \begin{bmatrix} x_r \\ x_a \end{bmatrix} + \begin{bmatrix} (E_r + A_{rf}K_6) \\ 0 \end{bmatrix} w \tag{63}$$

$$y = \begin{bmatrix} C_r + C_f K_4 & C_a + C_f K_5 \end{bmatrix} \begin{bmatrix} x_r \\ x_a \end{bmatrix} + (F_R + C_f K_6) w \tag{64}$$

We reduced all the aerodynamic lag states and chose to retain the first 10 modes, up to 29 Hz. We also retained only the hydraulic actuators (ailerons and flaperon) as they had a higher bandwidth than the electric actuators and would be more suitable for GLA control, especially at higher gust frequencies. The model was, therefore, reduced from an original 430 states, to 31 states. Fig. 6 and Fig. 7 depict the comparison between the original 430-state model and the reduced 31-state model. These responses are for the condition: Mach = 0.8, $q = 230\ lb/ft^2$, and 20 Hz gust frequency.

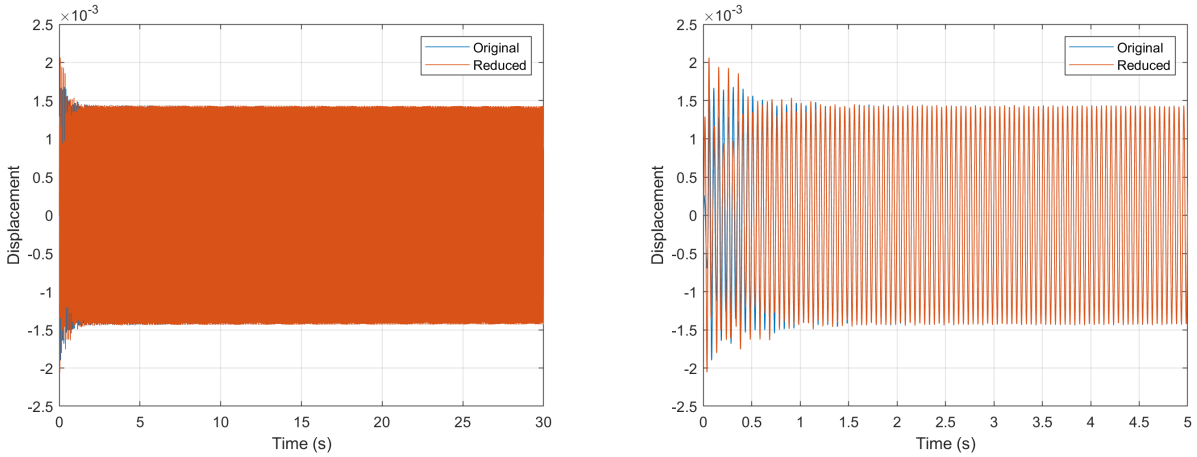

(a) $0 < t < 30$ (b) $0 < t < 5$

Figure 6 Reduced Model: State Comparison

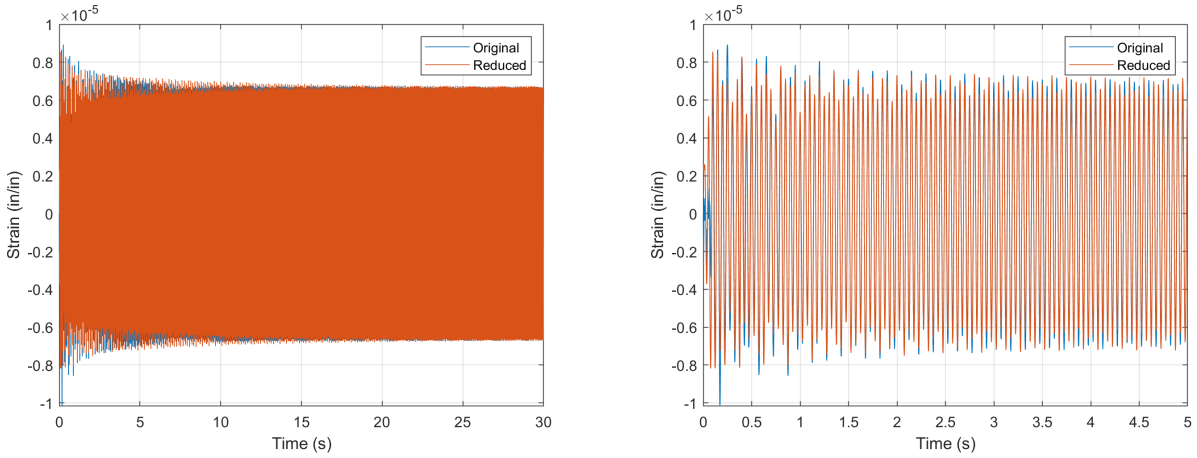

(a) $0 < t < 30$ (b) $0 < t < 5$

Figure 7 Reduced Model: Sensor Comparison

Fig. 6 depicts the response of state 10, which corresponds to the 10th structural mode displacement. We see perfect matching in the steady-state response with some disparity in the transient response. Fig. 7 depicts the response of the wing root strain sensor SG01. Similarly, we see perfect matching in the steady-state response and some disparity in the transient response. This is to be expected because for the model reduction we assume the steady-state response to be sinusoidal at the gust frequency, but the same is not true for the transient response, although there is still fair response matching in the transient response.

III. Gust Load Alleviation Controller

A. State Estimation and Gust Estimation

The AOS system in Transonic Dynamics Tunnel at NASA LaRC, produces a sinusoidal gust disturbance. We can take advantage that the gust signal is sinusoidal and write it as:

$$\dot{w} = \underbrace{\begin{bmatrix} 0 & 1 \\ -\omega^2 & 0 \end{bmatrix}}_{A_w} w \tag{65}$$

Where ω is the frequency of the sinusoidal disturbance, which will be known during testing. We can then formulate the extended-state system for purposes of estimating the disturbance,

$$\begin{bmatrix} \dot{x} \\ \dot{w} \end{bmatrix} = \begin{bmatrix} A & E \\ 0 & A_w \end{bmatrix} \begin{bmatrix} x \\ w \end{bmatrix} + \begin{bmatrix} B \\ 0 \end{bmatrix} u \tag{66}$$

$$y = \begin{bmatrix} C & F \end{bmatrix} \begin{bmatrix} x \\ w \end{bmatrix} \tag{67}$$

We then design a Kalman filter on the extended system.

The frequency of the gust, ω, may not be exactly at the prescribed frequency. In the final paper, we will investigate an adaptive estimation technique to accommodate uncertainty in the gust frequency.

B. Optimal Control

The GLA controller is developed using a multi-objective optimal control method with the cost function

$$J = \lim_{t_f \to \infty} \frac{1}{2} \int_0^{t_f} [\hat{x}^T Q \hat{x} + u^T R u + P^T Q_P P] \, dt \tag{68}$$

subject to

$$\dot{\hat{x}} = A\hat{x} + Bu + L(y - \hat{y}) \tag{69}$$

$$\hat{y} = C\hat{x} \tag{70}$$

and

$$P = P_{\hat{x}}\hat{x} \tag{71}$$

P is the estimated sensor output, in this case, it is the wing root strain gauge that we wish to minimize. $P_{\hat{x}}$ is the estimated-state contribution to the output P.

The Hamiltonian is formed:

$$H = \frac{1}{2}\hat{x}^T Q \hat{x} + \frac{1}{2} u^T R u + \frac{1}{2}\hat{x}^T P_{\hat{x}}^T Q_P P_{\hat{x}} \hat{x} + \lambda^T (A\hat{x} + Bu + L(y - \hat{y})) \tag{72}$$

$$H = \frac{1}{2}\hat{x}^T Q \hat{x} + \frac{1}{2} u^T R u + \frac{1}{2}\hat{x}^T P_{\hat{x}}^T Q_P P_{\hat{x}} \hat{x} + \lambda^T (A\hat{x} + Bu + L(y - C\hat{x})) \tag{73}$$

The conditions for optimality are:

$$\dot{\lambda} = -\frac{\partial H}{\partial \hat{x}}^T = -Q\hat{x} - P_{\hat{x}}^T Q_P P_{\hat{x}} \hat{x} - A^T \lambda + C^T L^T \lambda \tag{74}$$

$$\frac{\partial H}{\partial u} = Ru + B^T \lambda \tag{75}$$

The optimal control is then obtained as

$$u = -R^{-1} B^T \lambda \tag{76}$$

Let, $\lambda(t) = W(t)\hat{x}(t) + V(t)$. u then becomes

$$u = -R^{-1} B^T (W\hat{x} + V) = -R^{-1} B^T W\hat{x} - R^{-1} B^T V \tag{77}$$

Differentiating $\lambda(t)$ yields

$$\dot{\lambda} = \dot{W}\hat{x} + W\dot{\hat{x}} + \dot{V} = -Q\hat{x} - P_{\hat{x}}^T Q_P P_{\hat{x}} \hat{x} - A^T \lambda + C^T L^T \lambda \tag{78}$$

Substituting for $\dot{\hat{x}}$ and λ

$$\dot{W}\hat{x} + W(A\hat{x} + Bu + L(y - \hat{y})) + \dot{V} = -Q\hat{x} - P_{\hat{x}}^T Q_P P_{\hat{x}} \hat{x} - A^T (W\hat{x} + V) + C^T L^T (W\hat{x} + V) \tag{79}$$

Substituting for u

$$\dot{W}\hat{x} + W(A\hat{x} + B(-R^{-1} B^T W\hat{x} - R^{-1} B^T V) + L(y - \hat{y})) + \dot{V} = -Q\hat{x} - P_{\hat{x}}^T Q_P P_{\hat{x}} \hat{x} - A^T (W\hat{x} + V) + C^T L^T (W\hat{x} + V) \tag{80}$$

Upon expanding and reorganizing we obtain

$$\dot{W}\hat{x} + WA\hat{x} - WLC\hat{x} + A^T W\hat{x} - C^T L^T W\hat{x} - WBR^{-1} B^T W\hat{x} + A^T V - C^T L^T V - WBR^{-1} V + WLy + \dot{V} = -Q\hat{x} - P_{\hat{x}} Q_p P_{\hat{x}} \hat{x} \tag{81}$$

Let,

$$\bar{Q} = Q + P_{\hat{x}}^T Q_P P_{\hat{x}} \tag{82}$$

$$Q_y = -WL \tag{83}$$

$$\bar{A} = A - LC \tag{84}$$

Then,

$$\dot{W}\hat{x} + W\bar{A}\hat{x} + \bar{A}^T W\hat{x} - WBR^{-1} B^T W\hat{x} + \bar{Q}\hat{x} + (\bar{A}^T - WBR^{-1} B^T)V + \dot{V} = Q_y y \tag{85}$$

For infinite time horizon, $\dot{W} = 0$ and $\dot{V} = 0$. Then we obtain the modified Riccatti equation:

$$W\bar{A} + \bar{A}^T W - WBR^{-1} B^T W + \bar{Q} = 0 \tag{86}$$

and

$$V = (\bar{A}^T - WBR^{-1} B^T)^{-1} Q_y y \tag{87}$$

The control then becomes

$$u = -R^{-1} B^T W\hat{x} - R^{-1} B^T (\bar{A}^T - WBR^{-1} B^T) Q_y y \tag{88}$$

The control can be written as

$$u = K_{\hat{x}} \hat{x} + K_y y \tag{89}$$

Then

$$K_{\hat{x}} = -R^{-1} B^T W \tag{90}$$

$$K_y = -R^{-1} B^T (\bar{A}^T - WBR^{-1} B^T)^{-1} Q_y \tag{91}$$

IV. Stability Margin Analysis

It is of particular importance that the stability margins of the GLA controller be robust because the controller will be implemented on hardware, the CRM wind-tunnel model in the TDT. The ASE model developed is an analytical model and will likely not be a sufficiently accurate representation of the actual wind tunnel model. Prior to GLA controller testing, there will be a series of system identification and model validation tests to validate and make the necessary adjustments to the ASE model to improve the accuracy of the analytical model. Nonetheless, the controller needs to be able to accommodate reasonable uncertainties in the model to ensure stability.

Two approaches were used to analyze the stability margins. The first is loop-at-a-time (LAT) margins. We assess the stability margins in a single loop at a time while holding the other loops closed. Then, we find the worst-case gain and phase margins from all the loops. We can then compare the worst-case stability margins to other configurations of the controller to assess the relative robustness of different controller iterations.

To compute the loop at a time margins, we assemble the open-loop transfer functions of the controller and the plant. The transfer function of the plant is given by

$$G(s) = C(sI - A)^{-1}B \tag{92}$$

The transfer function of the controller, which is a state feedback controller with observer, is given by

$$D(s) = K_{\hat{x}}(sI - A + BK_{\hat{x}} + LC)^{-1}L \tag{93}$$

Thus, the open loop transfer function of the controller on the plant, at the plant input, is given by[13]

$$D(s)G(s) = K_{\hat{x}}(sI - A + BK_{\hat{x}} + LC)^{-1}LC(sI - A)^{-1}B \tag{94}$$

We also evaluate the stability margins at the plant output. This open-loop transfer function is given by[13]

$$G(s)D(s) = C(sI - A)^{-1}BK_{\hat{x}}(sI - A + BK_{\hat{x}} + LC)^{-1}L \tag{95}$$

We rapidly compute the stability margins using the MATLAB function $allmargin$ using the systems defined by Eq. 94 and Eq. 95.

As a second method of assessing the stability margins of the controller, the disk-based stability margins were evaluated at the plant input and plant output using the MATLAB Simulink Control System Tuner tool, which was used on a block diagram Simulink model of the plant and the controller. Disk-based margins evaluate the uncertainty in gain and phase in multiple loops simultaneously. As such, the results of the disk-based margin evaluation are much more conservative than the loop-at-a-time margins.

Using these methods to evaluate the robustness controller, different configurations of sensors were selected to assess the impact that sensor selection has on controller robustness. The sensor configuration is the set of sensors that the Extended Kalman Filter uses for the measurement update. Some considerations for sensor selection included total number of sensors used, location, and orientation. For instance, strain gauges will likely provide more information closer to the wing-root because the strain is lower near the tip than the root. Similarly, the acceleration near the root is lower than the acceleration near the tip.

The results of the stability analysis for 4 sets of sensors are depicted in the following tables. Table 1 depicts the stability margins at the plant input and Table 2 depicts the stability margins at the plant output. Lastly, Table 3 shows the performance for different configurations.

Table 1 Stability Margins at the Plant Input

Configuration	# of Sensors	LAT PM (°)	Disk PM (dB)	LAT GM (dB)	Disk GM (dB)
1	10	68.0	36.0	9.8	5.9
2	7	71.8	37.6	9.6	6.2
3	7	71.8	37.6	9.6	6.2
4	4	199.8	49.3	17.8	8.6

Table 2 Stability Margins at the Plant Output

Configuration	# of Sensors	LAT PM (°)	Disk PM (dB)	LAT GM (dB)	Disk GM (dB)
1	10	262.8	20.0	8.5	3.1
2	7	269.3	20.5	8.4	3.2
3	7	269.3	12.3	8.4	1.6
4	4	Inf	38.4	14.7	6.3

Table 3 Sensor Configuration and Performance

Configuration	% Strain Reduction
1	72.5
2	71.8
3	72.4
4	75.6

In Table 1, we see that configuration 4 shows the most robust gain and phase margins at the plant input. In Table 2, configuration 4 also shows the most robust gain and phase margins at the plant output. The sensor configuration is tied to the Kalman Filter, and therefore, the Kalman Filter gain L. Thus, the configuration of the sensor impacts the feedback gain, and therefore the performance. However, the impact is low compared to the differences in stability margins and can be seen in Table 3, where configuration 4 provides the most strain reduction. Therefore, based on the results shown in the previous tables, sensor configuration 4 was shown to have the most robust margins and is the sensor configuration chosen for the GLA controller. Fig. 8 and Fig. 9 depict the locations of the sensors in configuration 4. The sensors outlined in red are the ones used for this configuration.

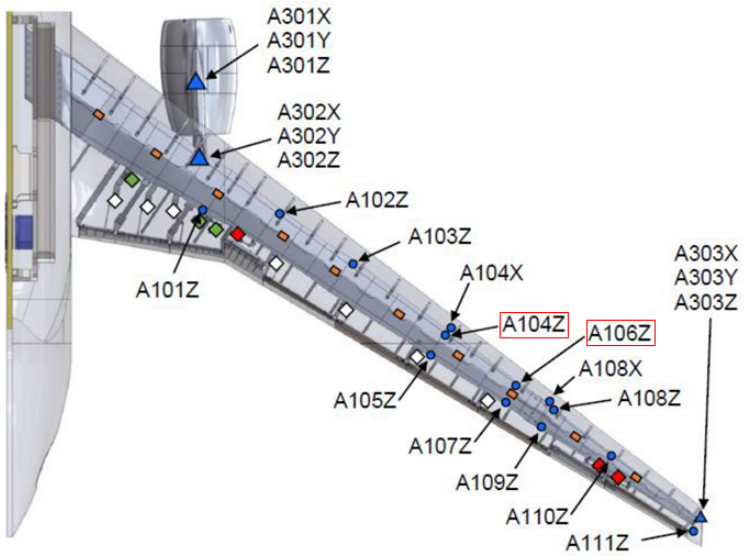

Figure 8 Acceleration Sensor Selection[3]

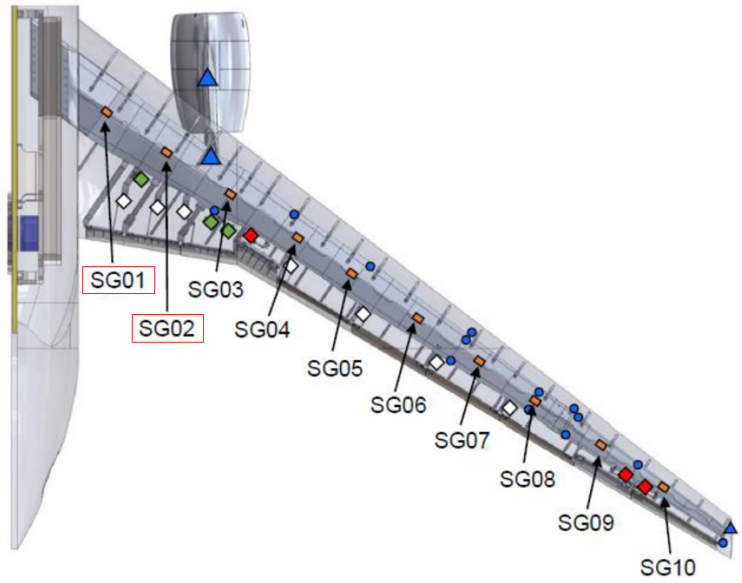

Figure 9 Strain Sensor Selection[3]

The tradeoff between stability margins is performance is also assessed. One way to accomplish this is by varying the R-matrix in the optimal control derivation, which is the term that weights the control effort. For varying R-matrix, the stability margins and strain reduction are found and reported in the following tables. R is varied from the baseline $R_0 = 0.004I$.

Table 4 Stability Margins at the Plant Input

R Value	LAT PM (°)	Disk PM (dB)	LAT GM (dB)	Disk GM (dB)
R_0	194.4	49.3	17.8	8.6
$R_0 * 0.1$	99.8	47.6	14.5	8.2
$R_0 * 5$	Inf	54.5	22.4	9.9
$R_0 * 10$	Inf	59.1	25.1	11.2

Table 5 Stability Margins at the Plant Output

R Value	LAT PM (°)	Disk PM (dB)	LAT GM (dB)	Disk GM (dB)
R_0	Inf	38.4	14.7	6.3
$R_0 * 0.1$	Inf	38.1	12.4	6.3
$R_0 * 5$	Inf	40.0	18.2	6.6
$R_0 * 10$	Inf	41.8	21.0	7.0

Table 6 Controller Tuning and Performance

R Value	% Strain Reduction
R_0	75.6
$R_0 * 0.1$	95.2
$R_0 * 5$	40.9
$R_0 * 10$	25.1

Tables 4, 5, and 6 depict the stability margins and performance of the controller for variations is the optimal control parameter, R. This parameter clearly has a large impact on performance, but a smaller impact on stability margins. Based off these results the tuning $R = R_0$ shows a good balance between robustness and performance and is the tuning setting chosen for this controller.

V. Simulation Results

A simulation was developed to test the GLA controller. The controller was designed using the reduced order ASE model, but was applied to the full order ASE model. The test condition was Mach = 0.8, $q = 230\ lb/in^2$, and $20Hz$ gust frequency. The following plots depict the performance of the controller with respect to strain reduction, and the performance of the extended Kalman filter estimation. Fig. 10 shows the comparison of the root strain signal for the GLA controller inactive, and GLA controller active. The magnitude of the strain, in the steady-state response with the GLA controller inactive, is $6.74x10^{-6}\ in/in$. With the GLA controller active, the strain is $1.64x10^{-6}\ in/in$. This is a reduction of $5.10x10^{-6}\ in/in$, or a 75.6% reduction.

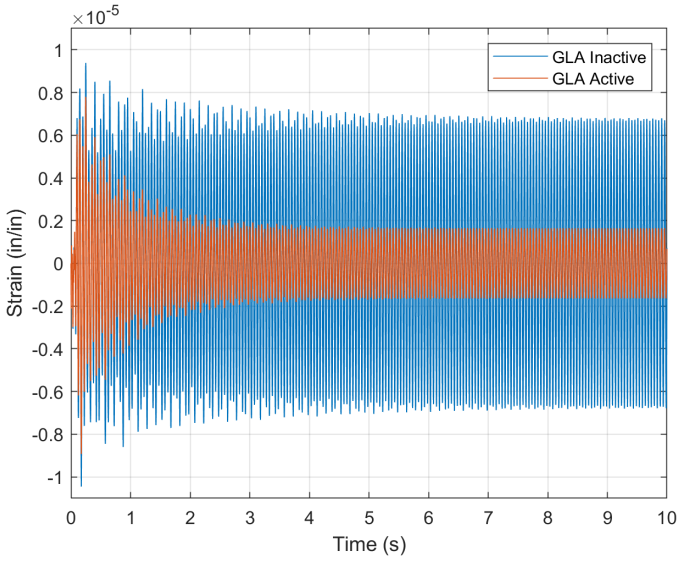

Figure 10 GLA Controller Performance

Fig. 11, 12, and 13 show the comparison between the system response and the estimated response for a senor (SG01), a gust state, and a modal state (first-t structural mode displacement). As seen in these plots, the estimated response converges around 3 seconds, and the steady-state response shows perfect matching.

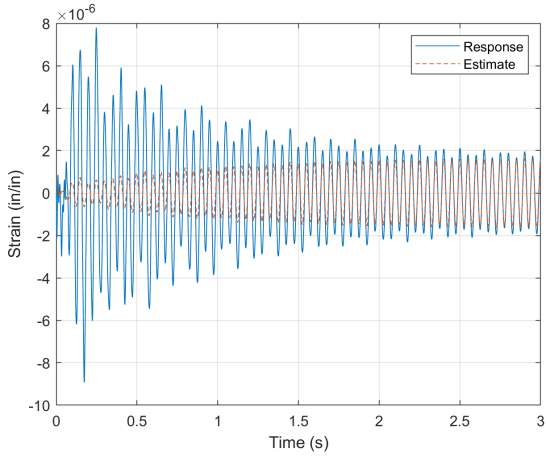

(a) $0 < t < 3$

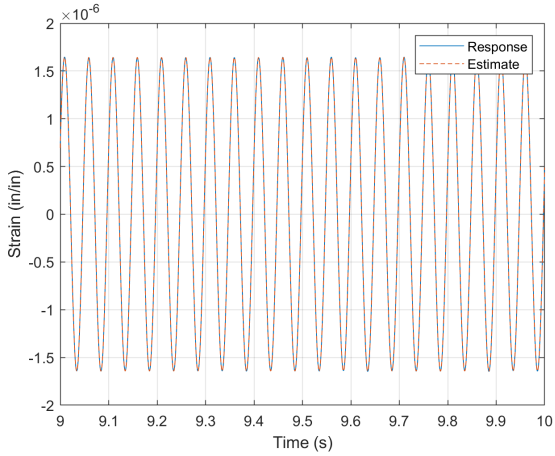

(b) $9 < t < 10$

Figure 11 Strain Estimate

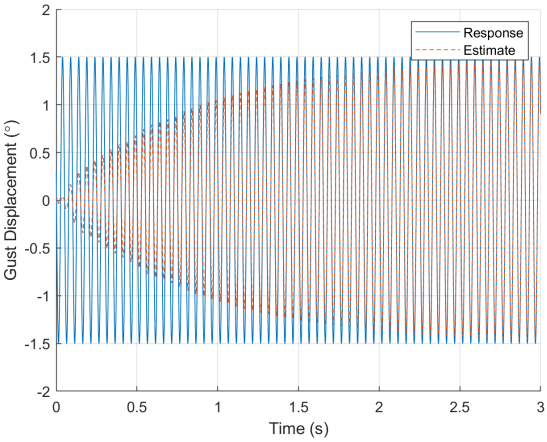

(a) $0 < t < 3$

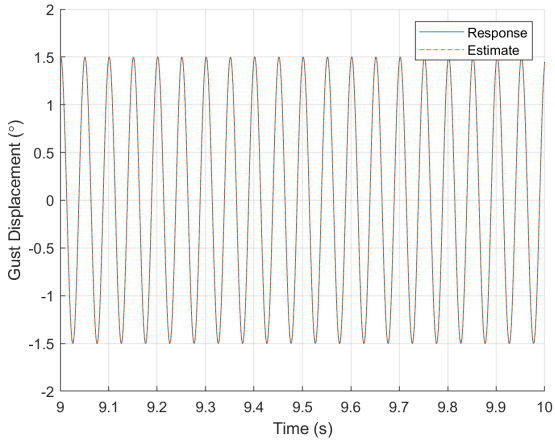

(b) $9 < t < 10$

Figure 12 Gust Estimate

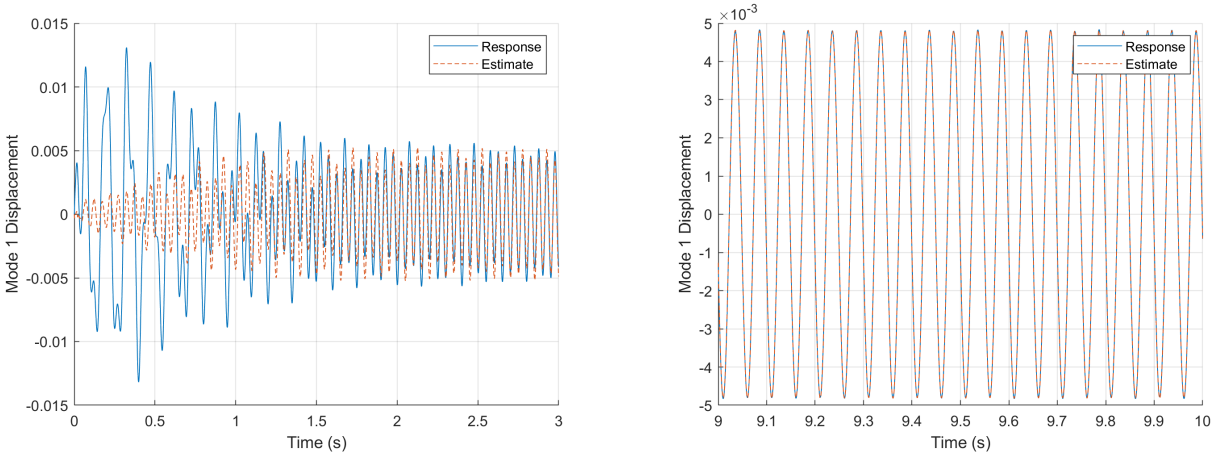

(a) $0 < t < 3$

(b) $9 < t < 10$

Figure 13 State Estimate

VI. Conclusions

This study presents the gust load alleviation controller design for the CRM wind-tunnel model, in preparation for wind-tunnel testing scheduled for late 2022. The aeroservolastic model was reduced using a technique that takes advantage of the sinusoidal response of the system given a sinusoidal gust input to the system. This reduction showed perfect matching in the steady-state response and some disparity in the transient response when comparing the full order ASE model with the reduced model. The extended-state system is defined and provides the framework for state and gust estimation. The system was then used to design an extended-state Kalman filter for estimation. The controller is derived from the optimal control solution to a multi-objective cost function. The stability margins of the controller were analyzed and used as a measure of robustness. This enabled the selection of a more optimal sensor set and the assessment of tradeoffs between robustness and performance.

The selected controller provided robust stability margins and good gust alleviation performance. The configuration selected provided loop-at-a-time (LAT) phase margins of 199.8° at the plant input and an infinite LAT phase margin at the plant output. The LAT gain margins are 17.8dB and 14.7dB at the input and output, respectively. The disk-based phase margin is 49.3° and 38.4° at the input and output, respectively. Lastly, the disk-based gain margins are 8.6dB and 6.3dB at the input and output, respectively. In simulation the controller enabled a reduction of 75.6% of the wing-root strain gauge signal. One significant finding was that it was necessary to have robust stability margins at the output, especially because there was slight mismatch in the transient response between the full ASE model and the reduced model used for controller design.

VII. To Be Completed in Final Manuscript

The final paper will consider performance with sensor noise, and uncertainty in gust frequency. An adaptive gust frequency estimation technique will be developed to accommodate the uncertainty.

Acknowledgment

The authors wish to acknowledge NASA Advanced Air Transport Technology (AATT) project for the funding support of this work. The authors also wish to acknowledge Boeing Research and Technology, in particular Dr. John Quindlen, for providing the aerodynamic data to support this work under NASA contract NNL15AA00A with the AATT project. The authors also wish to acknowledge NASA LaRC for providing the aeroservolastic models used in this study.

References

[1] Vassberg, J., Dehaan M., Rivers, M., and Wahls, R., "Development of a Common Research Model for Applied CFD Validation Studies," 26th AIAA Applied Aerodynamics Conference, AIAA-2008-6919, August 2008.

[2] Forte, C., Nguyen, N., Xiong, J., "Real-Time Drag Optimization and Maneuver Load Alleviation Control for a High Aspect Ratio Wing Wind Tunnel Model," AIAA SciTech 2022 Forum, AIAA 2022-0715, December 29, 2021.

[3] Boeing Research and Technology, "Integrated Adaptive Wing Technology Maturation Year 5 Review," February 2,2020.

[4] NASA Langley Research Center, "Transonics Dynamics Tunnel," https://aeroelasticity.larc.nasa.gov/facilities/transonic-dynamics-tunnel/.

[5] Hashemi, K., Nguyen, N., Drew, M., Chaparro, D., and Ting,E., "Performance Optimizing Gust Load Alleviation Control of Flexible Wing Aircraft," 2018 AIAA Guidance, Navigation, and Control Conference, AIAA 2018-0623, Jan 7, 2018.

[6] Nguyen, N., Hashemi, K., "Multi-Objective Flight Control for Ride Quality Improvement for Flexible Aircraft," AIAA SciTech 2020 Forum, AIAA 2020-1623, Jan 5, 2020.

[7] Nguyen. N., "Elastically Shaped Future Air Vehicle Concept," NASA Innovation Fund Award 2010 Report, October 2010, Submitted to NASA Innovative Partnerships Program, http://ntrs.nasa.gov/archive/nasa/casi.ntrs.nasa.gov/20110023698.pdf.

[8] Nguyen. N., and Urnes, J., "Aeroelastic Modeling of Elastically Shaped Aircraft Concept via Wing Shaping Control for Drag Reduction," AIAA Atmospheric Flight Mechanics Conference, AIAA-2012-4642, August 2012.

[9] Nguyen, N. and Tal, E., "A Multi-Objective Flight Control Approach for Performance Adaptive Aeroelastic Wing," 56th AIAA/ASME/ASCE/AHS/SC Structures, Structural Dynamics, and Materials Conference, AIAA-2015-1843, January 2015.

[10] Nguyen, N., Ting, E., Chaparro, D., Drew, M., and Swei, S., "Multi-Objective Flight Control for Drag Minimization and Load Alleviation of High-Aspect Ratio Flexible Wing Aircraft," 58th AIAA/ASME/ASCE/AHS/SC Structures, Structural Dynamics, and Materials Conference, AIAA-2017-1589, January 2017.

[11] Ferrier, Y., Nguyen, N., Ting, E., Chaparro, D., Wang, X., de Visser, C., and Chu, Q., "Active Gust Load Alleviation of High-Aspect Ratio Flexible Wing Aircraft," AIAA Guidance, Navigation, and Control Conference, AIAA-2018-0620, January 2017.

[12] Waite, J., Grauer, J., Bartels, R, Stanford, B., "Aeroservolastic Control Law Development for the Integrated Adaptive Wing Technology Maturation Wind-Tunnel Test," AIAA SciTech 2021 Forum, January 2021.

[13] Nguyen, N., "Applied Feedback Control," Lecture Notes, University of California Santa Cruz, March 2021.